Design Optimization of a Three Degrees-of-Freedom Variable-Reluctance Spherical Wrist Motor

R. B. Roth
HV Technologies, Inc.,
Trenton, GA 30752

Kok-Meng Lee
Associate Professor,
Georgia Institute of Technology,
Atlanta, GA 30332-0405

This paper presents the basis for optimizing the design of a three degrees-of-freedom (DOF) variable reluctance (VR) spherical motor which offers some attractive features by combining pitch, roll, and yaw motion in a single joint. The spherical wrist motor offers a major performance advantage in trajectory planning and control as compared to the popular three-consecutive-rotational joint wrist. Since an improved performance estimate is required, a method for optimizing the VR spherical motor's magnetics was developed. This paper begins with a presentation of the geometrical independent and dependent variables which fully described the design of a VR spherical motor. These variables are derived from examination of the torque prediction model. Next, a complete set of constraint equations governing geometry, thermal limitations, amplifier specifications, iron saturation, and leakage flux are derived. Finally, an example problem is presented where the motor's geometry is determined by maximizing the output torque at one rotor position. The concept of developing a spherical motor with uniform torque characteristics is discussed with respect to the optimization methodology. It is expected that the resulting analysis will improve the analytical torque prediction model by the inclusion of constraint equations, aid in developing future VR spherical motor designs, improve estimates of performance, and therefore will offer better insight into potential applications.

1 Introduction

The need to compete in the international marketplace has led manufacturers toward automation as one method of lowering costs and producing quality products and services. Small robot manipulators such as a robot wrist or hand have become necessary inventions for coordinate measurement, material handling, automated assembly systems, and laser machining. Present robot manipulator designs are constructed by arranging single degree-of-freedom motors in series and/or parallel connected by linkages. These systems have significant disadvantages since they tend to be larger in size and mass, have decreased positioning accuracy because of elastic deformation of gears and linkages, and may have singularities in their workspaces that is a major problem in trajectory planning and control. A ball-joint-like VR spherical motor which combines roll, yaw, and pitch motions in a single joint offers a major performance advantage in trajectory planning and control as compared to the popular three consecutive rotational joint wrist.

Recently, several design concepts of spherical motors for smooth and continuous motion have been proposed. A spherical induction motor was conceptualized in [1] for robotic applications and the detailed analysis was given in [2]. However, it is difficult to realize a prototype of its kind because of its complexity in mechanical and winding design and manufacturing. Hollis et al. [3] developed a six degree-of-freedom (DOF) wrist for fine motion actuation based on the principle of direct-current (DC) motor. Another DC spherical motor with three DOF in rotation was demonstrated by Kaneko et al. [4]. Although the DC spherical motor is characterized by its mechanical simplicity, the range of inclination and the torque constant are rather limited.

Lee et al. [5] proposed an alternative design of a spherical motor based on the concept of a variable reluctance (VR) stepper motor. Lee and Kwan [6] developed the theory based on the local interaction between the adjacent stator and rotor poles to demonstrate the concept feasibility of the spherical stepper motor. As compared with its DC counterpart, the spherical stepper motor has a relatively large range of motion, possesses isotropic inertial properties, and is simple and compact in design. The trade-off, however, is that a sophisticated switching scheme is required due to the large number of inputs and nonuniform distribution of poles. To allow a few but evenly spaced stator poles to be used for smooth motion control, Lee and Pei [7] analyzed the kinematic relationships between the stator and rotor poles which are located at the vertices of regular polyhedrons, and developed a method to examine the influences of the design configurations on motion feasibility. Lee and Wang [8] presented the dynamic model and control strategy of a VR spherical motor. To fully understand the potential performance capabilities and therefore applications, we present here a methodology for optimizing the magnetic system of a VR spherical motor.

The contributions of this paper may be summarized briefly as follows: (*1*) A complete set of geometrical independent and dependent variables are presented which fully described the VR spherical motor design. These variables are derived from examination of the analytical torque prediction model. (*2*) A complete set of constraint equations governing geometry, thermal limitations, amplifier specifications, iron saturation, and leakage flux are derived. (*3*) The resulting formulation is shown to be practical in implementation. A Generalized-Reduced Gradient (GRG) solver [9] was used to determine the "best" motor geometry by maximizing the output torque at any orientation.

The remaining paper is organized as follows: The operating principle of the VR spherical motor is briefly described in Sec-

Contributed by the Production Engineering Division for publication in the JOURNAL OF ENGINEERING FOR INDUSTRY. Manuscript received April 1993; revised March 1994. Associate Technical Editor: K. Danai.

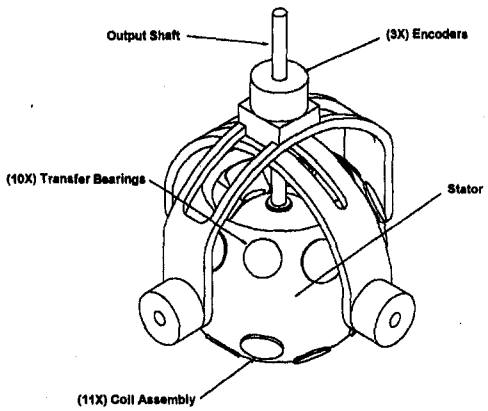

Fig. 1(*a*) Assembly view of a VR spherical motor

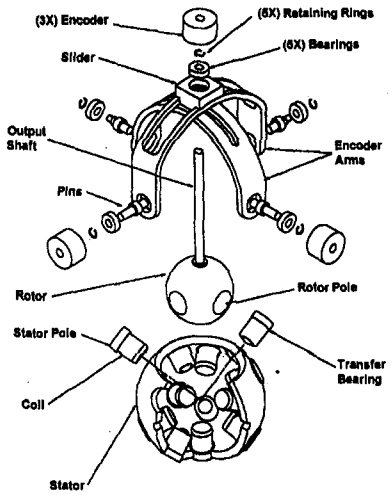

Fig. 1(*b*) Structure of a VR spherical motor

tion 2. Section 3 presents the list of independent and dependent variables that completely describe the VR spherical motor's geometry which were derived from the analytical torque prediction model. Potential motor configurations are examined by placing the poles at the vertices of regular polyhedra. Section 4 presents the necessary constraint equations governing the analytical model. Section 5 presents the optimization example where the motor geometry is determined by maximizing the motor's output torque. The formulation is discussed in conjunction with the goal of designing a spherical motor with uniform torque characteristics. Finally, conclusions are made in Section 6.

2 Operational Principle of a VR Spherical Motor

The VR spherical motor discussed here has a structure similar to that of a spherical stepper [6]. There are, however, two basic differences between the spherical stepper and the VR spherical motor: (*1*) Unlike the spherical stepper which has a constant-magnitude input to the stator poles, the stator pole inputs to the VR spherical motor can be independently varied. (*2*) Both the stator poles and rotor poles are evenly distributed on the spherical surfaces. As a result of these differences, the number of stator poles required for a VR spherical motor can be much smaller than that of a spherical stepper and the resolution of the VR spherical motor does not depend on having a large number of stator poles.

The VR spherical motor design consists of four basic subassemblies: namely, a stator, a rotor, bearings, and measuring mechanism as illustrated in Fig. 1(*a*) and Fig. 1(*b*). The spherical rotor and the hollow spherical stator are concentric and are supported one on the other by means of bearings. The rotor is made of a hard nonmagnetic material to provide a smooth spherical surface for the bearing rollers to support it with minimal friction. The poles on the stator, called stator poles, are wound by coils and each coil can be energized individually. The stator poles are strategically distributed on the stator surface. The points on which the stator poles are located form the vertices of a polyhedron. Pythagoras and Plato [10] have shown that a complex polyhedral angle must be made up of at least three faces and must be less than 360° to form a closed polyhedron. Using these principles, the maximum number of coils which can be evenly spaced on a sphere is 20. Similarly, the rotor poles are distributed on the rotor surface. The rotor poles meet at the center of the rotor, and the stator cores are connected by the magnetic conductor layer in the stator shell to form a magnetic circuit with the airgap. In order to maintain geometrical symmetry for simplicity in control, the stator poles and the rotor poles are of a circular shape. The kinematic relations governing the measuring mechanism which locates the rotor orientation with respect to the stator has been discussed in [7].

The spherical motor operates by the principle of variable reluctance. In the operation of the VR spherical motor, the stator coils are energized individually. A magnetic field is established which creates magnetic energy in the airgaps. The magnetic energy is a function of the relative position of the rotor and stator. The motion of the VR spherical motor is generated as the rotor tends to move to a position such that the energy in the airgap is minimized. For the purpose of modeling the VR spherical motor, the motor is considered to consist of three major components: namely, a set of m interconnecting stator poles, a set of n interconnecting rotor poles, and the air gaps formed between pairs of overlapped stator and rotor poles. The schematics of the electro-magnetic system is shown in Fig. 2. For a specific problem where the geometry, the material properties, and the boundary conditions are well defined, Maxwell's equations represent the distributed parameter model of the electro-magnetic system. The analytical torque model of the spherical motor used is a lumped-parameter approach analogous to the linear electric circuit. The linearized circuit model allows the flux flowing through the reluctance of airgaps to be considered separately.

The total output torque produced by the motor is determined by computing the individual torque contributions from each airgap element. The individual torque contribution from the airgap element between the ith stator pole and jth rotor pole has been previously derived in [8]:

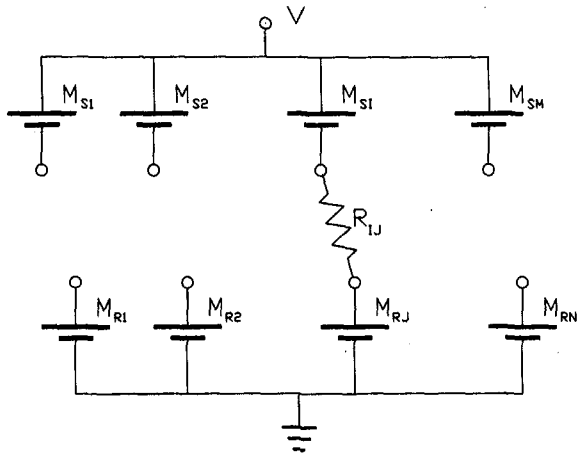

Fig. 2 Magnetic circuit of a VR spherical motor

$$\vec{\mathbf{t}}_{ij} = \frac{1}{2}(M_{si} + M_{rj} - V)^2 \frac{dP(\psi)}{d\psi}\bigg|_{\psi=\psi_{ij}} \vec{\mathbf{e}}_{ij} \quad (1)$$

where V, $\vec{\mathbf{e}}_{ij}$, and $P(\psi)$ are to be described. The electro-magnetic system of the VR spherical motor can be modeled as shown in Fig. 2. M_{si} and M_{rj} denote the magnetomotive forces (mmf's) generated by the ith stator pole and jth rotor pole, respectively. R_{ij} $(=1/P_{ij})$ denotes the reluctance of the airgap between the ith stator pole and the jth rotor pole, and Φ_{ij} is the corresponding flux flowing through R_{ij}. The magnetic potential of the magnetic conductor layer with respect to that at the center of the rotor is denoted as V. The magnetic potential V can be derived from Fig. 2 using the principles of linear circuit theory as

$$V = \sum_{i=1}^{m}\sum_{j=1}^{n} P_{ij}(M_{si} + M_{rj}) / \sum_{i=1}^{m}\sum_{j=1}^{n} P_{ij}. \quad (2)$$

We define the position vectors of the ith stator pole and jth rotor poles to be ${}^{xyz}\bar{r}_{si}$ and ${}^{xyz}\bar{r}_{rj}$, respectively, in the rotor reference frame. The unit vector $\vec{\mathbf{e}}_{ij}$ which is perpendicular to the position vectors ${}^{xyz}\bar{r}_{si}$ and ${}^{xyz}\bar{r}_{rj}$ is determined by

$$\vec{\mathbf{e}}_{ij} = \frac{{}^{xyz}\bar{r}_{si} \times {}^{xyz}\bar{r}_{rj}}{R^2 \sin \psi_{ij}} \quad (3)$$

where the angle between the ith stator pole and jth rotor pole is determined from the dot product of the position vectors as

$$\cos \psi_{ij} = \frac{{}^{xyz}\bar{r}_{si} \cdot {}^{xyz}\bar{r}_{rj}}{R^2} \quad (4)$$

and R is the mean radius of a spherical surface separating the pole faces of the stator and rotor.

The analytical torque model requires a model of the airgap permeance, $P(\psi)$. The airgap permeance model is a function of the relative displacement between an adjacent stator pole and rotor pole pair. The following airgap permeance model was used to illustrate the basic design principle,

$$P(\psi) = \frac{\mu_0 S(\psi)}{g} \quad (5)$$

where μ_0 is the magnetic permeability of free space, $S(\psi)$ is the overlapping area between an adjacent pole pair and g is the airgap dimension. This permeance model assumes (*1*) the flux passes through overlapping pole areas and (2) the flux through the overlapping area is uniform. This permeance model has the advantages of being relatively simple while allowing all pole sizes to be examined. Computational efficiency is required as the optimization software will call the analytical model several hundred thousand times in order to determine the optimal geometry. Since fringing flux has been neglected, the computed torque will be a conservative estimate of the actual torque. The disadvantage of the model is that the feasible pole size regions will tend to be conservative and the computed pole sizes may be larger than is necessary. Thus, Eqs. (1), (2), (3), (4), and a permeance model, $P(\psi)$, define the torque generated by the VR spherical motor for a given set of inputs in terms of the magnetomotive forces produced by the coils.

Table 1 Independent geometry variables

Independent Variable	Description
ψ_r	Rotor pole size
ψ_s	Stator pole size
R_r	Rotor radius
g	Air gap length
$l_{sp,cap}$	Length of the stator pole cap
$l_{rp,cap}$	Length of the rotor pole cap
$d_{wire,bare}$	Diameter of the bare wire
$d_{sp,in}$	Inside diameter of stator pole
$R_{st,in}$	Inside radius of the stator
$R_{st,out}$	Outside radius of the stator

Table 2 Dependent geometry variables

Dependent Variable	Description
$d_{sp,out}$	Effective outside diameter of stator pole
$d_{rp,in}$	Inside diameter of the rotor pole
l_{coil}	Length of stator pole coil
l_{thd}	Length of stator pole connected to stator
t_{sp}	Effective stator pole tooth thickness
t_{rp}	Effective rotor pole tooth thickness

3 Motor Geometry

In the previous section, the analytical torque prediction model was presented. In this section, the physical geometrical variables which significantly influence the torque generated by the VR spherical motor are identified. The variables are further separated into two categories: (*1*) independent variables and (*2*) dependent variables. A dependent variable is determined by examining the motor design itself and observing whether the variable can be written in terms of the independent variables imposed by the geometrical constraints. The set of independent variables fully describe the VR spherical motor design and therefore are the only ones which may be adjusted by the GRG solver in maximizing the objective function. Finally, different motor configurations are examined by placing the poles at the vertices of regular polyhedra.

3.1 Geometrical Variables. The following is a minimum set of parameters needed to compute the motor's output torque using the analytical torque prediction model and permeance model. The list includes the rotor radius, rotor position, airgap length, rotor and stator pole sizes, pole locations, magnetomotive force input (mmf), and rotor orientation. Several of these parameters describe the spherical motor's geometry, for example, the rotor radius, air gap dimension, pole locations, and the pole sizes. However, the motor's mmf input cannot be computed from these parameters alone requiring additional geometrical variables. A total of ten independent geometrical variables were identified and are summarized in Table 1. The dependent geometrical variables are summarized in Table 2. Each of the dependent geometrical variables may be expressed in terms of the independent variables. These relations are derived using trigonometry based on the geometry shown in Fig. 3 and Fig. 4 as

$$d_{sp,out} = 2(R_r + g + l_{sp,cap}) \tan \psi_s$$

$$d_{rp,in} = 2(R_r - l_{rp,cap}) \tan \psi_r$$

$$l_{coil} = \sqrt{R_{st,in}^2 - d_{sp,out}^2/4} - R_r - g - l_{sp,cap}$$

$$l_{thd} = \sqrt{R_{st,out}^2 - d_{sp,out}^2/4} - R_r - g - l_{sp,cap} - l_{coil}$$

$$t_{sp} = l_{sp,cap} + R_r + g - \sqrt{(R_r + g)^2 - d_{sp,in}^2/4}$$

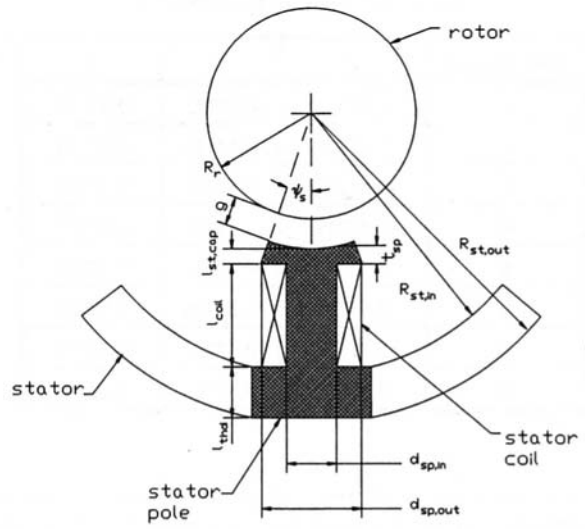

Fig. 3 Parameters associated with the spherical motor design

$$t_{rp} = l_{rp,in} + \sqrt{R_r^2 - d_{rp,in}^2/4} - R_r \qquad (6)$$

The rotor assembly in Fig. 4 does not show the rotor poles connection to the magnetic rotor core which is required to provide a complete magnetic flux path. The size of the rotor core is computed at the end of the optimization run by summing the flux passing through the core and sized to prevent iron saturation.

3.2 Pole Design. One of the key parts in optimizing the spherical motor's magnetics is the stator pole. Excitation of the stator pole results in the energizing force that causes the motor torque to be produced. The stator pole coil depends on the motor geometry in addition to the wire used. This section describes the stacking pattern used, determines the number of turns, and calculates the coil resistance based on the geometrical parameters.

Round copper wire was assumed for the construction of the stator pole coil. The bare wire diameter variable was treated as a continuous function in the simulation although in the physical sense, wire is typically available in discrete 0.5 gauge sizes. To prevent shorting, the wire must be insulated. An additional dependent variable is defined which is the diameter of the insulated wire, $d_{wire,insl}$. The insulated wire diameter is a nonlinear function that depends on the bare wire diameter. For purposes of the simulation, a table was constructed linking the insulated wire diameter to the bare wire diameter based on vendors' data sheets.

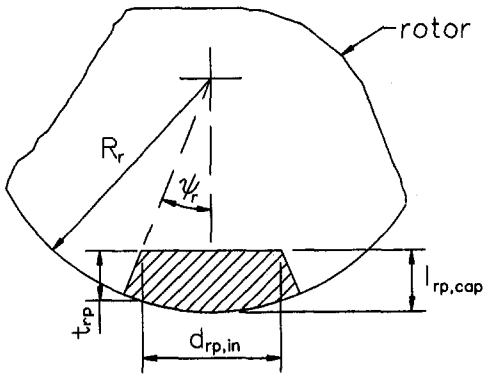

Fig. 4 Parameters associated with rotor assembly

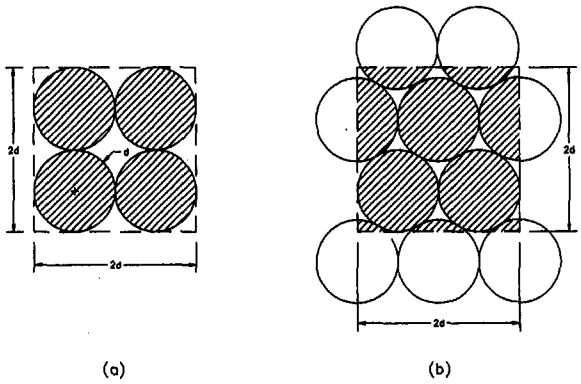

Fig. 5 Wire stacking methods

The stacking pattern used is shown in Fig. 5. Based on the geometrical parameters' defined and the stacking pattern, the magnetomotive force (mmf) input is computed. The mmf input from the ith stator pole is defined as the number of coil turns, N_{turns}, multiplied by the input current to the ith stator pole coil, I_i. The stator pole coil volume is bounded by the length of the coil, l_{coil}, the outside diameter of the stator pole, $d_{sp,out}$, and the inside diameter of the stator pole, $d_{sp,in}$. Based on this bounded volume, illustrated in Fig. 6, and making use of the INT function defined in FORTRAN compilers, the maximum number of coil layers is

$$n = \mathrm{INT}\left\{1 + \frac{2\sqrt{3}}{3}\left[\frac{d_{sp,out} - d_{sp,in}}{2d_{wire,insl}} - 1\right]\right\}. \qquad (7)$$

The number of coil turns can also be obtained from Fig. 6. If the number of layers is an even number, the total number of wire turns is

$$N_{turns} = \frac{n}{2}\left\{\mathrm{INT}\left(\frac{l_{coil}}{d_{wire,insl}}\right) + \mathrm{INT}\left(\frac{2l_{coil} - d_{wire,insl}}{2d_{wire,insl}}\right)\right\}. \qquad (8)$$

If the number of layers is an odd number, the total number of wire turns is

$$N_{turns} = \left(\frac{n+1}{2}\right)\left(\mathrm{INT}\left[\frac{l_{coil}}{d_{wire,insl}}\right]\right) + \left(\frac{n-1}{2}\right)\left(\mathrm{INT}\left[\frac{2l_{coil} - d_{wire,insl}}{2d_{wire,insl}}\right]\right). \qquad (9)$$

Thus, Eqs. (7), (8), and (9) provide a means to compute the number of turns on a stator pole from the motor geometry.

3.3 Motor Configurations. This section examines possible stator and rotor pole configurations by placing the poles at the vertices of regular polyhedrons. Constraint equations are developed which depend on the analytical torque model which ensure that no magnetic singularities exist within the motor's workspace.

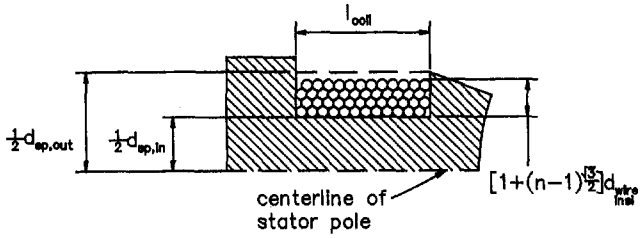

Fig. 6 Stator pole coil volume

Table 3 Pole locations for tetrahedron

Pole Number	X	Y	Z
1	0.94281	0	0.333333
2	-0.47140	0.81650	0.333333
3	-0.47140	-0.81650	0.333333
4	0	0	-1

3.3.1 Pole Configurations. For simplicity, it is desirable that the poles are circular and evenly spaced on the stator and rotor following the pattern of regular polyhedrons. Each vertex of the polyhedron corresponds to the location of one pole. The regular polyhedrons of tetrahedron, octahedron, hexahedron, icosahedron, and dodecahedron correspond to four, six, eight, twelve, and twenty vertices, respectively. The location of the vertices are summarized in Tables 3 through 7. To ensure torque generation in any rotational direction, the number of stator poles, M, must not equal the number of rotor poles, N, since a minimum reluctance state occurs when all poles align and no torque can be generated, that is

$$M \neq N. \tag{10}$$

For manufacturing simplicity, the design should minimize the number of poles in the rotor. On the other hand, high resolution demands more poles. This demand is met by placing more poles on the stator. Consequently, there must be more stator poles than rotor poles,

$$M > N. \tag{11}$$

These two restrictions reduces the number of potential design configurations from twenty-five to ten.

In evaluating the remaining configurations, the stator configurations are modified to maximize the workspace as follows: The octahedron configuration was reduced by one by removing the top most pole (pole #5). The hexahedron configuration was used unaltered. The icosahedron configuration was reduced by one by removing the top pole (pole #11). Finally, the dodecahedron configuration was reduced by five by removing the top most ring (poles #1–5). As illustrated in Fig. 7, the maximum motor inclination that can be achieved due to stator pole interference is

$$\Gamma = 90 - \alpha - \psi_s, \tag{12}$$

where ψ_s is the stator pole size and α is the angle of inclination of the top most stator pole with respect to the xy plane. The α values are given for the different design configurations in Table 8.

Table 4 Pole locations for octahedron

Pole Number	X	Y	Z
1	1	0	0
2	0	1	0
3	-1	0	0
4	0	-1	0
5	0	0	1
6	0	0	-1

Table 5 Pole locations for hexahedron

Pole Number	X	Y	Z
1	0.57735	-0.57735	0.57735
2	0.57735	0.57735	0.57735
3	-0.57735	0.57735	0.57735
4	-0.57735	-0.57735	0.57735
5	0.57735	-0.57735	-0.57735
6	0.57735	0.57735	-0.57735
7	-0.57735	0.57735	-0.57735
8	-0.57735	-0.57735	-0.57735

3.3.2 Maximum Pole Size. A geometric bound exists on the maximum rotor and stator pole size possible. The largest rotor pole size allowable is when two adjacent poles touch,

$$\psi_{r,\max} = \tfrac{1}{2}\cos^{-1}({}^{xyz}\bar{r}_{rj} \cdot {}^{xyz}\bar{r}_{rk}), \quad j \neq k, \tag{13}$$

where ${}^{xyz}\bar{\mathbf{r}}_{rj}$ and ${}^{xyz}\bar{\mathbf{r}}_{rk}$ are the position vectors of two adjacent rotor poles in the reference system attached to the rotor. A similar formulation exists for the maximum stator pole size,

$$\psi_{s,\max} = \tfrac{1}{2}\cos^{-1}({}^{XYZ}\bar{r}_{sj} \cdot {}^{XYZ}\bar{r}_{sk}), \quad j \neq k, \tag{14}$$

where ${}^{XYZ}\bar{\mathbf{r}}_{sj}$ and ${}^{XYZ}\bar{\mathbf{r}}_{sk}$ are the position vectors of two adjacent stator poles in the reference system attached to the stator. Table 9 summarizes the maximum pole sizes for the different configurations.

3.3.3 Determining the Feasible Pole Sizes. A singular point in the workspace is a point where degrees of freedom are reduced. In the spherical motor design, there are no interior mechanical singularities in the workspace. However, there are possible electromagnetic singularities. A electromagnetic singularity is defined as a point where the magnetic field is unable of producing torque in all possible directions regardless of coil excitation. The feasible rotor and stator pole size combinations are now determined for the remaining design configurations. A feasible combination is defined as being free of singularities

Table 6 Pole locations for icosahedron

Pole Number	X	Y	Z
1	0.89442	0	0.44721
2	0.27639	0.85065	0.44721
3	-0.72361	0.52573	0.44721
4	-0.72361	-0.52573	0.44721
5	0.27639	-0.85065	0.44721
6	-0.89443	0	-0.44721
7	-0.27639	-0.85065	-0.44721
8	0.72360	-0.52573	-0.44721
9	0.72360	0.52573	-0.44721
10	-0.27639	0.85065	-0.44721
11	0	0	1
12	0	0	-1

Table 7 Pole locations for dodecahedron

Pole Number	X	Y	Z
1	0.49115	0.35684	0.79462
2	0.18760	0.57738	0.79462
3	-0.60710	0	0.79462
4	-0.18760	-0.57738	0.79462
5	0.49115	-0.35684	0.79462
6	0.79466	0.57735	0.18755
7	-0.30353	0.93418	0.18755
8	-0.98225	0	0.18755
9	-0.30353	-0.93418	0.18755
10	0.79466	-0.57735	0.18755
11	0.30353	0.93418	-0.18755
12	-0.79466	0.57735	-0.18755
13	-0.79466	-0.57735	-0.18755
14	0.30353	-0.93418	-0.18755
15	0.98225	0	-0.18755
16	0.18760	0.57738	-0.79463
17	-0.49115	0.35684	-0.79463
18	-0.49115	-0.35684	-0.79463
19	0.18760	-0.57738	-0.79463
20	0.60709	0	-0.79463

within the motor's operating workspace. This objective is achieved by meshing the entire workspace into a three-dimensional grid. Each grid point is examined to see whether torques can be generated along all six orthogonal directions.

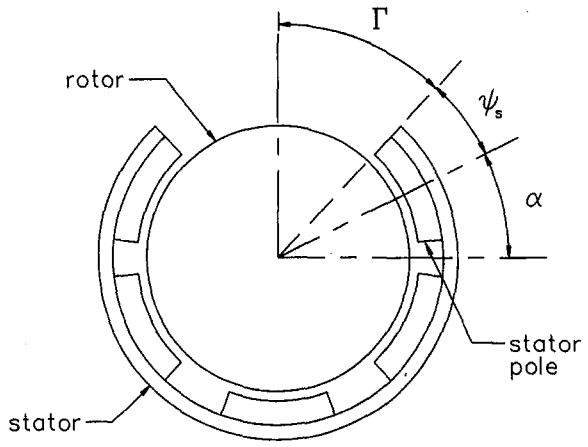

Fig. 7 Maximum range of inclination due to stator pole

The work space of the spherical motor is a three-dimensional space. In order to examine the work space, Z YZ Euler angles are adopted. The Z YZ Euler angles describe the rotor orientation in terms of a rotation ϕ_e about the z-axis, then a rotation θ_e about the new y-axis, y', and finally a rotation ψ_e about the new z-axis, z''. The work space of the motor can be written in terms of the Z YZ Euler angles as

$$0 < \phi_e < 2\pi,$$
$$0 < \theta_e < \Gamma,$$
$$0 < \psi_e < \pi, \tag{15}$$

where Γ is the maximum motor inclination. Given the three Z YZ Euler angles, the orientation of the rotor with respect to the stator can be obtained as

$$^{XYZ}T_{xyz} = \begin{bmatrix} c\phi_e c\theta_e c\psi_e - s\phi_e s\psi_e & -c\phi_e c\theta_e s\psi_e - s\phi_e c\psi_e & c\phi_e s\theta_e \\ s\phi_e c\theta_e c\psi_e + c\phi_e s\psi_e & -s\phi_e c\theta_e s\psi_e + c\phi_e c\psi_e & s\phi_e s\theta_e \\ -s\theta_e c\psi_e & s\theta_e s\psi_e & c\theta_e \end{bmatrix}. \tag{16}$$

It is more convenient to determine the motor's output torque in the rotor frame of reference. The location of the kth stator pole is obtained in the rotor frame of reference as

$$^{xyz}\bar{r}_{sk} = (^{XYZ}T_{xyz})^T\, ^{XYZ}\bar{r}_{sk}. \tag{17}$$

For any rotor orientation $(\phi_e, \theta_e, \psi_e)$, the kth stator pole generates a torque in $\mathbb{R}^3$,

$$\nu_k = K_k \sum_{j=1}^{n_{rp}} \left| \frac{\partial P_{jk}}{\partial \psi_{jk}} \right| \frac{(^{xyz}\bar{r}_{rj} \times {}^{xyz}\bar{r}_{sk})}{\| ^{xyz}\bar{r}_{rj} \times {}^{xyz}\bar{r}_{sk} \|}, \tag{18}$$

where K_k is a nonnegative torque constant dependent on geometry and mmf excitation. The permeance derivative for the overlapping area permeance model is nonzero when

$$|\psi_r - \psi_s| < \cos^{-1}(^{xyz}\bar{r}_{rj} \cdot {}^{xyz}\bar{r}_{sk}) < (\psi_r + \psi_s). \tag{19}$$

Now, consider a set of vectors $\{\nu_1, \nu_2, \ldots, \nu_k\}$. The set of vectors ν_k are determined by evaluating Eq. (18) for all stator poles in a particular motor design. The set V, which is the directional capacity of the spherical motor, consists of the nonnegative combinations of the ν_k,

$$V = (V \in \mathbb{R}^3, V = \sum_{k=1}^{n_{sp}} \alpha_k \nu_k, \alpha_k \geq 0). \tag{20}$$

In order to show that a particular grid point is not a singularity, V must generate $\mathbb{R}^3$.

THEOREM: The set V generates $\mathbb{R}^3$ if the vectors, ν_k, are shown to generate *all* the vectors, w_j, $j = 1, 2, \ldots, 6$, where the w_j are defined as

$$w_1 = \begin{bmatrix} 1 \\ 0 \\ 0 \end{bmatrix}, w_2 = \begin{bmatrix} 0 \\ 1 \\ 0 \end{bmatrix}, w_3 = \begin{bmatrix} 0 \\ 0 \\ 1 \end{bmatrix}, w_4 = \begin{bmatrix} -1 \\ 0 \\ 0 \end{bmatrix},$$
$$w_5 = \begin{bmatrix} 0 \\ -1 \\ 0 \end{bmatrix}, w_6 = \begin{bmatrix} 0 \\ 0 \\ -1 \end{bmatrix}. \tag{21}$$

PROOF: The theorem is proved by showing that the set of w_j generate $\mathbb{R}^3$. If the set of vectors, ν_k, generate all the w_j, then by the Transitive Axiom of Equality, V also generates $\mathbb{R}^3$. The set w_j are shown to generate $\mathbb{R}^3$ by dividing $\mathbb{R}^3$ into eight subspaces. The lower bounds of the eight subspaces are given by the following sets of generating vectors $\{w_1, w_2, w_3\}$, $\{w_2, w_3, w_4\}$, $\{w_3, w_4, w_5\}$, $\{w_1, w_3, w_5\}$, $\{w_1, w_2, w_6\}$, $\{w_2, w_4, w_6\}$, $\{w_4, w_5, w_6\}$, and $\{w_1, w_5, w_6\}$. These sets of vectors generate each subspace since some nonnegative combination of the w_j can reach any point in the particular subspace QED.

The following method was developed in order to demonstrate that the ν_k generate the w_j at a specific grid point. The w_j have been shown to generate $\mathbb{R}^3$. By demonstrating that the ν_k from

Table 8 Values for α

Polyhedron Model	Number of Stator Poles	α in degrees
Octahedron	6 (5)	0
Hexahedron	8	45
Icosahedron	12 (11)	26.565
Dodecahedron	20 / 15	52.62 / 10.81

Eq. (18) generates all the vectors, w_j, the set V has been shown to equal $\mathbb{R}^3$. Specifically, the following six subproblems must be shown to be true,

$$\sum_{k=1}^{n_{sp}} \alpha_{jk}\nu_k = w_j, \quad \alpha_{jk} \geq 0, \quad j = 1, 2, 3, 4, 5, 6. \tag{22}$$

A grid point is shown to have an electromagnetic singularity when any of the subproblems has no solution. The motor will be unable to generate torque in the direction of the generating vector in the unsolved case. This method requires the use of a linear equation solver for each subproblem using only three ν_k at a time. The coefficients, α_{jk}, are then examined to ensure that they are nonnegative.

REMARK: At any rotor position, the minimum number of stator poles required to generate torque in $\mathbb{R}^3$ is at least four. This conclusion is made the example of the generating vector set $V = (\{1, 0, 0\}^T, \{0, 1, 0\}^T, \{0, 0, 1\}^T, \{-1, -1, -1\}^T)$. The minimum number of required stator poles may be greater than four as illustrated by the set of six vectors, w_j.

In the implementation of this algorithm, the work space is meshed into a three-dimensional work space with a finite number of points. A program was written to examine all the grid points for singularities for the remaining ten design configurations with a one degree grid spacing. Due to motor symmetry, the actual work spaced examined is

$$\begin{aligned} 0 < \phi_e < \phi_{e,\max}, \\ 0 < \theta_e < \Gamma, \\ 0 < \psi_e < \psi_{e,\max} \end{aligned} \tag{23}$$

where the values of $\phi_{e,\max}$ and $\psi_{e,\max}$ depend on the number of stator and rotor poles, respectively. These values are summarized in Table 10.

The pole sizes examined for each design configuration were in the bounds of $0 < \psi_r < \psi_{r,\max}$ and $0 < \psi_s < \psi_{s,\max}$. Two of the ten configurations were found to have significant feasible pole size regions using the overlapping area permeance. These two configurations are the 15/4 and 15/6 designs. The configuration which resulted in the largest motor workspace was the 15/6 configuration which results in a rotor inclination of approximately 45 degrees. The results from the grid search were bounded conservatively by linear equations as

$$\begin{aligned} 17.5° \leq \psi_s \leq 20.5° \\ 23.5° \leq \psi_r \leq 35.0° \\ \psi_r + 2.5\psi_s - 74.75 \geq 0 \\ \psi_r + 5.5\psi_s - 130.25 \geq 0 \end{aligned} \tag{24}$$

REMARK: The overlapping area permeance estimation is a conservative estimate. The neglecting of fringing flux in the permeance estimate can lead to the elimination of potential design configuration and pole sizes that are feasible.

4 Constraints

Constraint equations arise from the following: (*1*) physical constraints, (*2*) analytical model constraints, and (*3*) manufacturing constraints. Physical constraints arise from restrictions on geometry, bearings, and thermal limitations. Model constraints arise from assumptions made when deriving the analytical torque prediction model. For example, the analytical model neglects fringing flux, iron saturation, and assumes an ideal amplifier. To prevent incorrect model results, constraint equations are developed which in essence prevents the model from estimating the torque for a motor design that is saturated or has significant flux leakage. Manufacturing constraints are due to limits in manufacturing a part or assembly. For example, a lower limitation might be placed on the airgap dimension due to machining tolerances on the rotor and pole surfaces. For the VR spherical motor design, constraints governing geometry, thermal limitations, bearings, amplifier, iron saturation, and leakage flux are presented and discussed.

4.1 Geometry. All the independent variables listed in Table 1 are physical quantities and must be nonnegative. An additional four inequalities constraints are required to ensure that the motor's design configuration is preserved,

$$d_{\text{sp,out}} - d_{\text{sp,in}} \geq 0 \tag{25a}$$

$$R_r - l_{\text{rp,cap}} \geq 0 \tag{25b}$$

$$l_{\text{coil}} \geq 0 \tag{25c}$$

$$l_{\text{thd}} \geq 0 \tag{25d}$$

Physically, the motor design configuration is preserved by Eqs. (25*a*) through (25*d*) as follows: Equation (25*a*) places an upper limit on the inside diameter of the stator pole which is an independent variable since it cannot be greater than the outside diameter of the stator pole. Equation (25*b*) requires the length of the rotor pole cap to be smaller than the rotor radius which also ensures that the inside diameter of the rotor pole is nonnegative. Equation (25*c*) ensures that rotor radius is contained within the stator spherical shell. Equation (25*d*) ensures that the inside stator radius must be smaller than the outside stator radius.

Table 9 Maximum pole sizes

Vertices	$\psi_{\max}$ (degrees)
4	54.74
6	45
8	35.26
12	31.72
20	20.9

Table 10 Values for $\phi_{e,\max}$ and $\psi_{e,\max}$

Design Configuration	Values for $\phi_{e,\max}$ and $\psi_{e,\max}$ (degrees)
Tetrahedron	120
Octahedron	90
Hexahedron	90
Icosahedron	72
Dodecahedron	72

4.2 Bearing System. The requirements of the bearing system design for a VR spherical motor are as follows: (*1*) The bearing system should be small and compact in order to conserve space for the stator poles. (*2*) The bearing should be made from a material of low magnetic permeability so as to minimize the effect on the magnetic fluxes. (*3*) The bearings should be able to handle large loads due to pole attraction. (*4*) The bearing deflection under such loading should be small so as to minimize the change in airgap dimension.

From these requirements, three constraint equations are derived for a theoretical bearing system for the VR spherical motor design: (*1*) physical size, (*2*) maximum loading force, and (*3*) maximum bearing deflection. The first constraint governs the physical size of the bearing. Two possibilities exist for the placement of the bearings within the spherical motor design. The first possibility would place the individual bearings between the stator poles mounted to the inside stator wall to support the rotor. Referring to Fig. 9, the size constraint of a bearing placed between two adjacent stator poles is

$$2\psi_s + \psi_b \leq \Lambda_s \tag{26}$$

where ψ_s is the stator pole half angle size, Λ_s is the angle between adjacent stator poles, and ψ_b defines the occupying size of the bearing.

The second constraint places a restriction on the maximum loading force on the individual bearing. The majority of the bearing loading is due to the magnetic attraction forces between an adjacent stator pole-rotor pole pair that occurs when a stator pole is energized. The maximum bearing loading due to pole attraction depends on the pole configuration, motor dimensions, rotor orientation, and excitation levels. Once a worse case scenario is computed, the maximum loading due to pole attraction is required to be much smaller than the maximum bearing load allowable,

$$|F_{\substack{\text{magnetic}\\\text{loading}}}| \leq |F_{\substack{\text{bearing}\\\text{allowable}}}|. \tag{27}$$

Within the VR spherical motor design, the airgap length must be maintained to minimize changes in the airgap permeance model. Thus, the maximum bearing deflection is required to be much smaller than the airgap dimension. Like the maximum force computation, the worse case bearing deflection must be computed for a particular configuration. We require that the maximum bearing deflection must be much smaller than the airgap dimension or

$$y_{\substack{\max\\\text{deflection}}} \leq N_{\text{deflect}} g, \tag{28}$$

where N_{deflect} is a large number. Thus, Eqs. (26), (27), and (28) define the bearing constraint equations.

4.3 Thermal. Limitations on the stator pole current are required usually due to an upper temperature limit on the wire insulation. One method of defining a thermal limit is to specifying a maximum current density. Thus, an inequality constraint defining the maximum coil current is defined for the ith stator pole coil as

$$\frac{4|I_i|}{\pi d^2_{\text{wire,bare}}} \leq J_{\max} \tag{29}$$

where J_{max} is the maximum current density. The maximum current density ratings are given in [10] for different motor environments and are summarized in Table 11.

4.4 Amplifier. The current amplifier's specification can affect the spherical motor's design. A current amplifier typically has a maximum current rating, power rating, and voltage rating. Constraint equations are developed governing the amplifier current, power rating, and electrical time constant.

Three different forms governing the maximum current that may be generated by the amplifier are developed. In the first case, the current to the ith stator pole coil required cannot exceed the maximum amplifier current rating. In the second case, the current to the ith stator pole cannot exceed the voltage rating developed by the amplifier. Finally, the electrical power required to energize the ith stator pole cannot exceed the power rating of the amplifier. These three cases are summarized as follows

$$|I_i| \leq I_{\text{amp,max}}, \tag{30a}$$

$$|I_i| \leq V_{\text{amp}}/R_{\text{coil}}, \quad \text{and} \tag{30b}$$

$$I_i \leq \sqrt{P_{\text{amp}}/R_{\text{coil}}}. \tag{30c}$$

Table 11 Current density ratings

Current Density (A/mm^2)	Description of Environment
1.55	Standard for closed wound enclosed coils
7.55	Nominal upper limit for field windings for fully enclosed armatures
15.5	Nominal upper limit for air-cooled windings
23.3	Upper limit for well-ventilated armature on open-type motor

The analytical torque model developed is a steady-state model. It ignores the dynamic response that occurs when a stator pole coil is first energized. To ensure fast torque response, a constraint is placed on the electrical time characteristics of the system. We required that the actual current time be less than the maximum rise time specified, $t_{\max}$, resulting in the constraint

$$t_{\max} \geq -\frac{L_{\text{coil}}}{R_{\text{coil}}} LN_e\left(1 - \frac{R_{\text{coil}} I_d}{V_{\text{amp}}}\right). \tag{31}$$

where L_{coil} and R_{coil} are the coil's inductance and resistance, respectively.

4.5 Saturation. The linear circuit model assumes that the iron reluctance is negligible relative to the air gap elements. When the iron begins to saturate, the analytical torque model overpredicts the actual motor torque output. Constraint equations are developed by computing the amount of flux passing through a critical region and ensuring that the flux density level remains below a flux density maximum. The maximum value used is determined by examination of the iron material's B-H curve.

The motor's flux path is divided into the following regions: (*1*) stator, (*2*) long portion of the stator pole excluding the tooth section, (*3*) stator pole tooth, (*4*) rotor pole tooth, (*5*) long portion of the rotor pole excluding the tooth section, and (*6*) rotor core. Constraint equations that prevent iron saturation were written for regions (1) through (5) since their geometries must be critically determined.

This section will use the geometry variables previously developed. It is assumed that the linear magnetic circuit has been solved representing the spherical motor's magnetics. From the circuit solution, Φ_{ij} is determined which is physically the flux passing from the ith stator pole to the jth rotor pole. Furthermore, Φ_{ij} may be further subdivided into the two components, $\Phi_{ij} = \Phi_{i,j-ol1} + \Phi_{i,j-ol2} = \Phi_{i-ol1,j} + \Phi_{i-ol2,j}$, which are the estimated fluxes passing through the partial overlapping areas defined in Fig. 8. $\Phi_{i,j-ol1}$ and $\Phi_{i,j-ol2}$ are the fluxes passing through the partial overlapping areas A_{ol1} and A_{ol2} of the stator pole, respectively. Likewise, $\Phi_{iol1,j}$ and $\Phi_{i-ol2,j}$ are the fluxes passing the partial overlapping areas A_{ol1} and A_{ol2} of the rotor pole, respectively.

The first critical region to be examined occurs between the stator pole and stator. To prevent saturation of the interface

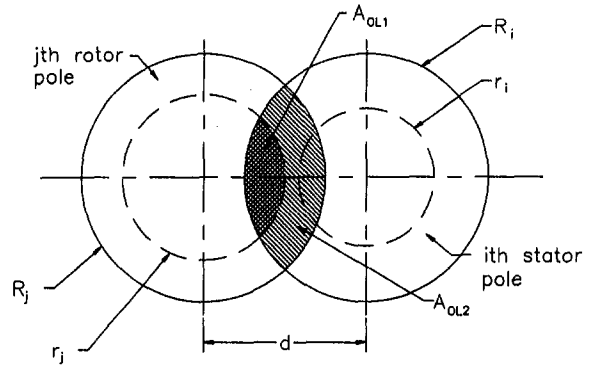

Fig. 8 Tooth geometry

between the ith stator pole and the stator, a maximum flux density level, B_{max}, is defined as

$$B_{max} \geq \frac{|\sum_j \Phi_{ij}|}{\pi d_{sp,in} l_{thd}}. \quad (32)$$

The next critical region occurs in the cross-sectional area of the long portion of the ith stator pole. To prevent saturation, a maximum flux density level is defined as

$$B_{max} \geq \frac{4|\sum_j \Phi_{ij}|}{\pi d_{sp,in}^2}. \quad (33)$$

Similarly, a critical region occurs in the cross-sectional area of the long portion of the jth rotor pole. To prevent saturation, a maximum flux density level is defined as

$$B_{max} \geq \frac{4|\sum_i \Phi_{ij}|}{\pi d_{rp,in}^2}. \quad (34)$$

The next critical region occurs in the ith stator pole tooth region which is the transition point between the stator pole tooth and the long portion of the stator pole. To prevent saturation in this region, a maximum flux density level is defined as

$$B_{max} \geq \frac{\sum_j |\Phi_{i,j-ol2}|}{\pi d_{sp,in} t_{sp}}. \quad (35)$$

Similarly, a critical region occurs in the jth rotor pole tooth region which is the transition point between the rotor pole tooth and the long portion of the rotor pole. To prevent saturation in this region, a maximum flux density level is defined as

$$B_{max} \geq \frac{\sum_i |\Phi_{i-ol2,j}|}{\pi d_{rp,in} t_{rp}}. \quad (36)$$

For the five regions, a total of $3m + 2n$ inequality constraints are defined where m is the number of stator poles and n is the number of rotor poles. In order to minimize the number of constraint equations due to leakage flux, one might attempt to restrict the flux density for the maximum value computed for each critical region, i.e.,

$$B_{max} \geq \text{MAX}\,[f_1(x), f_2(x), f_3(x), \ldots, f_n(x)]. \quad (37)$$

This idea leads to discontinuous derivatives of the constraint equations at $f_i = f_j$, $i \neq j$, which can lead to convergence problems for the optimization software.

4.6 Leakage Flux. The overlapping area permeance model assumes that there is no leakage flux in the motor design. Leakage flux can be minimized by ensuring that possible leakage flux paths are much longer than the desirable flux paths between an adjacent rotor and stator pole. Three possible leakage paths were identified in a spherical motor design: (*1*) adjacent stator poles, (*2*) adjacent rotor poles, and (*3*) bottom of stator pole tooth to inside stator radius. Constraint equations will be developed in this section that minimize the leakage flux associated with these flux paths.

A possible leakage path exists between adjacent stator poles. This leakage path is illustrated in Fig. 9. The empty radial angle between adjacent stator poles is $\Lambda_s - 2\psi_s$ where Λ_s is the angle between adjacent stator poles and ψ_s is the stator pole size. The smallest arc length between adjacent stator poles is $(R_r + g)(\Lambda_s - 2\psi_s)$. We require that the distance between the two adjacent stator poles to be much larger than the airgap dimension,

$$(R_r + g)(\Lambda_s - 2\psi_s) \geq N_{leakage} g \quad (38)$$

where $N_{leakage}$ is a large number. A similar leakage path exists between adjacent rotor poles resulting in the constraint equation

$$R_r(\Lambda_r - 2\psi_r) \geq N_{leakage} g. \quad (39)$$

The last leakage path is from the bottom of the stator pole tooth to the inside of the stator. Leakage flux is minimized by making this distance much larger than the airgap dimension. This requirement gives the constraint equation

$$R_{st,in} - [(\tfrac{1}{2} d_{sp,out})^2 + (R_r + g + l_{sp,cap})^2]^{1/2} \geq N_{leakage} g. \quad (40)$$

Thus, Equations (38), (39), and (40) define the leakage path restrictions for the analytical torque model.

5 Optimization Example

This section presents the optimization example using the analytical torque prediction model. The geometrical variables of a VR spherical motor design were determined by maximizing the output torque at one rotor orientation. Since the intended use of the spherical motor is as a robotic wrist manipulator, it is desirable to maximize the motor's output torque. This choice results in a design which provides a large payload capacity in addition to rapid acceleration capabilities. Thus, the following objective function, z, was used,

$$\max z = |T_x| + |T_y| + |T_z|. \quad (41)$$

In preliminary studies, the sum of the absolute values of the torque components was found to give better results than the sum of the squared torque output. This objective function, as defined by Eq. (41), results in designs that have more uniform torque characteristics. To ensure that the analytical torque model outputs were reasonable, the outside stator radius was fixed as $R_{st,out} = 76.2$ mm which is identical to the VR spherical motor

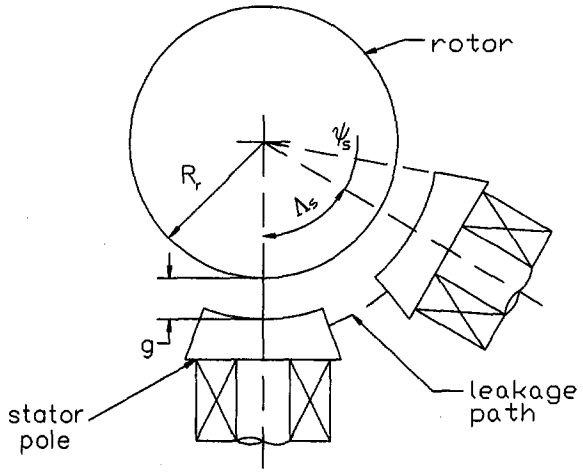

Fig. 9 Leakage path between adjacent stator poles

prototype upon which experimental torque measurements have been taken.

In addition to the nine independent geometric variables, fifteen independent variables are necessary to represent the current inputs to the stator poles. All variable constraints were written as $x_{lk} \leq x_k \leq x_{uk}$, where x_{lk} and x_{uk} are the lower and upper limits for the kth variable. The variable constraints were scaled so that their nominal magnitudes were on the order of 20 to 50 with respect to the optimization subroutine. The constraint equations implemented included geometry, thermal limitations, amplifier current limits, iron saturation, pole size limitations due to singularities, and leakage flux. The bearing design was neglected as the intent was to focus on the potential torque performance of the VR spherical motor. A thermal limitation was imposed by placing a current density limit of 7.55 Amps/mm^2 on the design. A flux density limit of 2.1 Wb/m^2 was used which assumes the use of high-performance iron. The current to the stator pole was limited to 5 Amps due to the amplifier limit on the experimental hardware setup. The leakage flux parameter, N_{leakage}, was set to 5 which is commonly used for motor and actuator design. A lower mechanical limit of 0.1 mm was placed on the airgap dimension. All constraint equations were written in terms of inequalities ($0 \leq g_j(x) \leq \infty$) and scaled so their magnitudes were on the order of 20 to 50 initially. The variable and constraint equations are summarized as follows:

$$
\begin{aligned}
23^\circ &\leq \psi_r \leq 35^\circ \\
17.5^\circ &\leq \psi_s \leq 20.5^\circ \\
-5 &\leq i_k \leq +5 \text{ amps}, \; k = 1, \ldots, 15 \\
0 &\leq R_r \leq 76.2 \text{ mm} \\
0.1 &\leq g \leq 76.2 \text{ mm} \\
0 &\leq l_{\text{sp,cap}} \leq 76.2 \text{ mm} \\
0 &\leq l_{\text{rp,cap}} \leq 76.2 \text{ mm} \\
0.2413 &\leq d_{\text{wire,bare}} \leq 2.588 \text{ mm} \\
0 &\leq d_{\text{sp,in}} \leq 76.2 \text{ mm} \\
0 &\leq R_{\text{st,in}} \leq 76.2 \text{ mm} \\
76.2 &\leq R_{\text{st,out}} \leq 76.2 \text{ mm (fixed)} \\
0 &\leq d_{\text{sp,out}} - d_{\text{sp,in}} \leq \infty \\
0 &\leq R_r - l_{\text{rp,cap}} \leq \infty \\
0 &\leq l_{\text{coil}} \leq \infty \\
0 &\leq l_{\text{thd}} \leq \infty \\
0 &\leq \psi_r + 2.5\psi_s - 74.75 \leq \infty \\
0 &\leq \psi_r + 5.5\psi_s - 130.25 \leq \infty \\
0 &\leq (R_r + g)(41.81 - 2\psi_s)\pi/180 - N_{\text{leakage}} g \leq \infty \\
0 &\leq R_r(90 - 2\psi_r)\pi/180 - N_{\text{leakage}} g \leq \infty \\
0 &\leq R_{\text{st,in}} - \sqrt{d_{\text{sp,out}}^2/4 + (R_r + g + l_{\text{sp,cap}})^2} \\
&\qquad - N_{\text{leakage}} g \leq \infty \\
0 &\leq J_{\max}\pi d_{\text{wire,bare}}^2 - 4i_k \leq \infty, \; k = 1, \ldots, 15 \\
0 &\leq B_{\max}\pi d_{\text{sp,in}}^2 - 4\left|\sum_j \Phi_{kj}\right| \leq \infty, \; k = 1, \ldots, 15 \\
0 &\leq B_{\max}\pi d_{\text{sp,in}} l_{\text{thd}} - \left|\sum_j \Phi_{kj}\right| \leq \infty, \; k = 1, \ldots, 15 \\
0 &\leq B_{\max}\pi d_{\text{rp,in}}^2 - 4\left|\sum_j \Phi_{kj}\right| \leq \infty, \; j = 1, \ldots, 6 \\
0 &\leq B_{\max}\pi d_{\text{sp,in}} t_{\text{sp}} - \sum_k |\Phi_{ij-ol2}| \leq \infty, \; j = 1, \ldots, 6 \\
0 &\leq B_{\max}\pi d_{\text{rp,in}} t_{\text{rp}} - \sum_k \sum_j |\Phi_{k-ol2,j}| \leq \infty, \; k = 1, \ldots, 15
\end{aligned}
\tag{42}
$$

Table 12 Initial conditions for optimization example

Description	Initial Conditions
i_1 through i_{15} (amps)	(1) 0.5, -0.5, 0.5, -0.5, 0.5, -0.5, 0.5, -0.5, 0.5, -0.5, 0.5, -0.5, 0.5, -0.5, 0.5 (2) 0.5, 0.5, -0.5, -0.5, 0.5, 0.5, -0.5, -0.5, 0.5, 0.5, -0.5, -0.5, 0.5, 0.5, -0.5 (3) 0.5, 0.5, 0.5, -0.5, -0.5, -0.5, 0.5, 0.5, 0.5, -0.5, -0.5, -0.5, 0.5, -0.5, 0.5 (4) 0.5, -0.5, 0.5, 0.5, -0.5, -0.5, -0.5, -0.5, 0.5, 0.5, 0.5, 0.5, -0.5, -0.5, -0.5
$d_{\text{wire,bare}}$ (mm)	0.4572 , 0.5842 , 0.7112, 0.8382
ψ_r (degrees)	29 , 31.5 , 34
$d_{\text{sp,in}}$ (mm)	19.05 , 22.86
g (mm)	0.4 , 0.5 , 0.6
$l_{\text{sp,cap}}$, $l_{\text{rp,cap}}$ $R_{\text{st,in}}$ (mm)	(1) 11.1125, 11.1125, 68.58 (2) 14.2875, 14.2875, 67.31
ψ_s (degrees)	18.75
R_r (mm)	38.1
$R_{\text{st,out}}$ (mm)	76.2 (fixed)

Since the objective function and many of the constraint equations are nonlinear, the optimization software will find only local optimal solutions. To find a global optimal solution, it is necessary to run the solver with different initial conditions. A total of $3^{24} = 2.82 \times 10^{11}$ optimization runs would be necessary if each variable was assigned three different initial conditions. Instead, a finite number of runs were made with the variables set with the initial conditions in Table 12. The total number of optimization runs was a more reasonable 576. These initial conditions were determined by preliminary studies. The geometric initial conditions were chosen to give a wide variation of the motor geometry without violating the geometry constraint equations. The initial conditions for the currents were based on reluctance motor operation which operates with pole pairs wired in series with opposite polarity to ensure a complete magnetic circuit. As a result, the analytical torque model was solved over one million times with 576 initial conditions and 3000 optimization calls per run on average.

The Generalized Reduced Gradient package was used to solve the nonlinear constrained optimization problem. As illustrated by Sandgren [12], GRG codes are robust, fast, and less sensitive to scaling problems. The "near" optimal results are given in Table 13. The objective function value was $z = 18$. Total run time for the 576 cases was approximately one week for an Intel 80486-33 MHz PC. Significant time improvement is expected by the use of a more efficient compiler and engineering workstation. Table 14 gives a synopsis of the nine geometrical variables and their relationships to the objective function and constraint equations. For example, the stator pole diameter is influenced by conflicting constraint equations. Increasing the stator pole diameter allows more flux to pass through the region before reaching magnetic saturation. Decreasing the stator pole diameter increases the stator pole coil size resulting in a greater

Table 13 "Near" optimal parameter values

Independent Variable	Description	Value
ψ_r	Rotor pole size (degrees)	29.3
ψ_s	Stator pole size (degrees)	19
R_r	Rotor radius (mm)	42
g	Air gap length (mm)	0.17
$l_{\text{sp,cap}}$	Length of the stator pole cap (mm)	14
$l_{\text{rp,cap}}$	Length of the rotor pole cap (mm)	10.5
$d_{\text{wire,bare}}$	Diameter of the bare wire (AWG)/(mm)	18.5 / 0.9652
$d_{\text{sp,in}}$	Inside diameter of stator pole (mm)	24.5
$R_{\text{st,in}}$	Inside radius of the stator (mm)	70
$R_{\text{st,out}}$	Outside radius of the stator (mm)	76.2

Table 14 Geometrical parameter trade-offs

Variable	Reasons to Increase	Reasons to Decrease
R_r	Increase moment arm, increase overlapping area, and decrease fringing flux between adjacent poles	Decreasing radius allows more room for other components
$R_{st,in}$	Leaves more room for other components	Prevent saturation of the stator
$d_{wire,bare}$	Larger current allowable	Increase number of wire turns for stator pole coil
$d_{sp,in}$	Prevent saturation	Allows more room for stator pole coil
$l_{sp,cap}$	Prevent saturation of stator pole tooth and allow for larger stator pole coil.	Leave more room for other components.
$l_{rp,cap}$	Prevent saturation of rotor pole tooth	Prevent saturation of rotor pole inner diameter
g	Prevent saturation and mechanical constraints	Lower current required for same output torque
ψ_s	Prevent saturation, allows for larger stator pole coil, and increase overlapping area	Prevent leakage flux, leave room for other components
ψ_r	Prevent saturation and increase overlapping area	Prevent leakage flux

magnetomotive force for the same current input. The best design occurs when the limits on flux density and thermal limits are reached, provided that all other constraints have been satisfied. From the results combined with physical insight, a better understanding of the parameter relationships associated with the design of a VR spherical motor are gained.

For comparison purposes, the performance of the "optimal" design was compared with the VR spherical motor prototype. Both motor were simulated at the upright position to determine the relative cost of generating a torque of 1 N-m about the z-axis. The new objective function which was minimized was

$$\min z = N[T_x^2 + T_y^2 + (T_d - T_z)^2] + R_{\text{coil}} \sum_{k=1}^{m} i_k^2 \quad (43)$$

where T_x, T_y, and T_z are the simulated torques about the x, y, and z-axes, N was a large number (10^7), T_d was 1 N-m, i_k was the current input to the kth stator pole, and R_{coil} is the stator pole resistance. This objective function will have a minimum when the simulated torque is equal to the desired torque at the lowest power input to the system. The computed objective function values for the optimal design and prototype design were 13.4 and 202.1, respectively. The total input power required by the optimal design is an order of magnitude lower than the prototype design, hence, it is more efficient. In addition, the flux density levels in the optimal design are lower than the prototype's indicating the motor can operate in the linear region of the magnetic material for higher torque levels. Similar results were obtained at additional positions and desired torques.

The goal of designing a VR spherical motor with uniform torque characteristics can be summarized by the phrase, "Maximize the minimum torque generated by the motor." One method of accomplishing this goal is by optimizing the output torque in different directions at several positions concurrently. This problem lends itself to parallel computer processing techniques. Current research is focused on identifying the direction and positions of the minimum torque vector for different motor configurations.

6 Conclusions

A complete set of geometrical independent, dependent variables, and pole configurations which fully describe the design of a VR spherical motor was presented in this paper. These variables were derived from examination of the torque prediction model. In addition, a complete set of constraint equations governing geometry, thermal limitations, amplifier specifications, iron saturation, and leakage flux were presented. Many of these same constraint equations will find use during control-law implementation which also utilizes the same analytical torque model.

The resulting formulation was shown to be practical in implementation. This was demonstrated by using a GRG solver to determine the "best" motor geometry by maximizing the output torque at one position. A minimal set of initial conditions was determined in order find a near "optimal" solution. The resulting design was compared with the prototype design and shown to be more efficient. It is expected the formulation presented here will serve as an effective tool for the performance analysis and the design of future VR spherical motors.

Acknowledgments

This work is supported by the National Science Foundation under grant numbers DMC 8810146 and DDM-8958383.

References

1 Vachtsevanos, G. J., Davey, K., and Lee, K-M., 1987, "Development of a Novel Intelligent Robotic Manipulator," *IEEE Control Systems Magazine,* pp. 9–15.

2 Davey, K., and Vachtsevanos, G., 1987, "The Analysis of Fields and Torques in a Spherical Induction Motor," *IEE Trans. on Magnetics,* Vol. MAG-23, pp. 273–282.

3 Hollis, R. L., Allan, A. P., and Salcudan, S., 1987, "A Six Degrees-of-Freedom Magnetically Levitated Variable Compliance Fine Motion Wrist," *The Fourth International Symposium on Robotics Research,* Santa Cruz, August.

4 Kaneko, K., Yamada, I., and Itao, K., 1988, "A Spherical DC Servo Motor with Three Degrees-of-Freedom," ASME *Dynamic Systems and Controls Division,* Vol. 11, pp. 398–402.

5 Lee, K-M., Vachtsevanos, G., and Kwan, C. E., 1988, "Development of a Spherical Stepper Wrist Motor," *IEEE International Conference on Robotics and Automation,* Philadelphia. Also in *Journal of Intelligent and Robotic Systems,* pp. 225–242.

6 Lee, K-M., and Kwan, C-K., 1991, "Design Concept Development of a Spherical Stepper Wrist Motor," *IEEE Journal of Robotics and Automation.*

7 Lee, K-M., and Pei, J., 1991, "Kinematic Analysis of a Three Degrees-of-Freedom Spherical Wrist Actuator," *The Fifth International Conference on Advanced Robotics,* Pisa, Italy, June 20–22.

8 Lee, K. M., and Wang, Xiao-An, 1992, "Development of a Variable-Reluctance Spherical Motor," *Proceedings of the 1992 NSF Grantees Conference,* Atlanta, GA, January 8–12.

9 Abadie, J., and Carpentier, J., 1969, "Generalization of the Wolfe Reduced Gradient Method to the Case of Nonlinear Constraints," *Optimization,* Academic Press.

10 Smith, D. E., 1923, *Essentials of Plane and Solid Geometry,* Wentworth-Smith Mathematical Series.

11 Warring, R. H., 1967, *Sub-Miniature Electric Motors,* Arco Publishing, London.

12 Sandgren, E., 1977, "The Utility of Nonlinear Programming Algorithms," Ph.D. dissertation, Purdue University, University Microfilm, doc. no. 7813115.